Simulations of recoil trajectories in Dubna Gas-Filled Recoil Separator 2 by GEANT4 toolkit

D.I. Solovyev[∗] **and N.D. Kovrizhnykh**

Joint Institute for Nuclear Research,
141980 Dubna, Russian Federation

E-mail: dmitri.solov@gmail.com

Abstract: Dubna Gas-Filled Recoil Separator (DGFRS-2) is a new facility at the Super Heavy Element Factory which allows us to study the properties of superheavy elements (SHEs) formed in complete fusion reactions in the femtobarn cross-section range. High dispersion and complex magnetic configuration make it difficult to tune the separator and find the optimal current values in the magnetic elements. This work presents a simulation model of the DGFRS-2 based on a GEANT4 toolkit. The main methods of trajectory simulations of heavy ions in gaseous media are discussed and several new processes are implemented in GEANT4. Calculation results agreed well with the data produced in test experiments which allows us to use this model for transmission determination and tuning of the separator in experiments aimed at SHE investigations.

[∗]Corresponding author.

Contents

1 Introduction

Superheavy elements are produced in complete fusion reactions of ions with target nuclei, leading to the formation of a compound nucleus followed by an evaporation of one or more neutrons. The heaviest elements with $Z = 113$–118 were synthesized in hot fusion reactions of ^{48}Ca ions with actinide isotopes. Cross sections of such reactions are usually in the range of several picobarns, which at an ion beam intensity of 10^{13} s^{-1} corresponds to the production rate of SHEs from 1 atom per month to 1 atom per day [1–3].

For further physical and chemical studies of SHEs, Super Heavy Element Factory (SHE Factory) was constructed at FLNR JINR. The facility is based on a new DC280 heavy-ion accelerator that can deliver ^{48}Ca beams with a design intensity of $6*10^{13}$ ions per second [4]. The first experimental setup of the SHE Factory is a Dubna Gas-Filled Recoil Separator 2 (DGFRS-2) with a $Q_v D_h Q_h Q_v D$ magnetic configuration. Figure 1 shows a schematic view of the separator. The first quadrupole Q1 focuses evaporation residues (ERs) recoiling from the target in the vertical direction in order to increase their transmission through a gap of a dipole magnet D1 [5]. The dipole magnet D1 focuses ERs in the horizontal direction and suppresses beam particles and the bulk of other background particles (such as scattered target nuclei, products of incomplete fusion, etc.). The Q2 and Q3 quadrupoles focus ERs at the focal plane of the separator in horizontal and vertical directions, respectively. A dipole magnet D2 reduces the background from high-energy charged particles, for instance, protons or α particles, which can be produced in the target and other parts of the separator and pass through D1 because of their high magnetic rigidity.
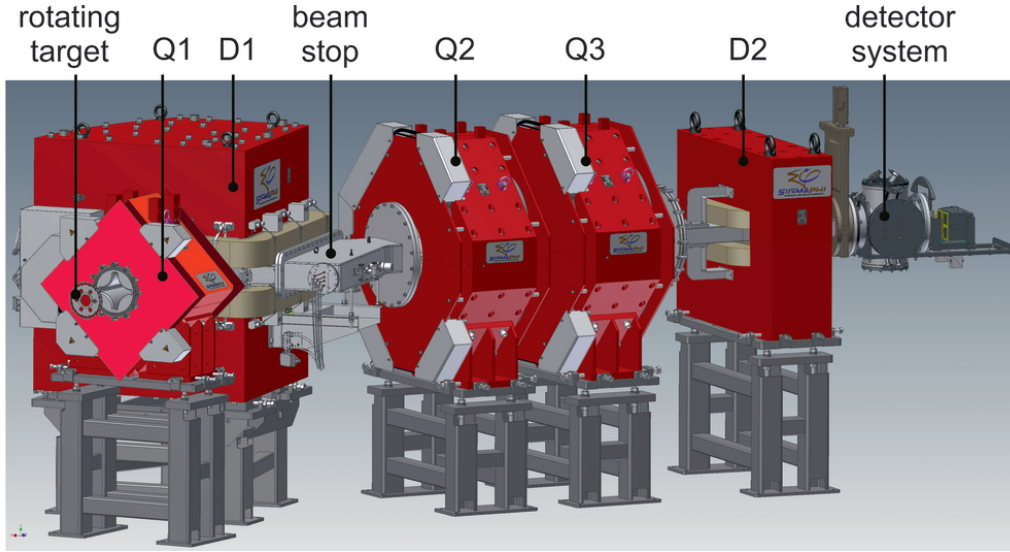
Figure 1. Schematic of the gas-filled separator DGFRS-2: a rotating target, magnets (Q1, D1, Q2, Q3, D2), a beam-stop chamber, and a detector chamber are shown.

In comparison to DGFRS-1, tuning of the new separator is more complicated because this setup comprises an increased number of magnetic components. Thus, in order to achieve maximum collection efficiency of ERs at the focal plane, it is necessary to simulate ER trajectories in the DGFRS-2 chamber and find the optimal field values in magnetic elements. GEANT4 [6] was chosen for its flexibility, a variety of implemented physics processes, and an ability to handle complex geometries.

2 DGFRS-2 operation principle

ER trajectories in a uniform magnetic field are determined by the expression:

$$B\rho = \frac{m\upsilon}{q},\tag{2.1}$$

where ρ is a radius of the ERs curvature; m, v, and q are their mass, velocity, and charge, respectively; B is a component of the magnetic field perpendicular to the ER velocity.

The expressions written in the left and right parts of equation (2.1) are called the magnetic rigidity of the separator and ERs, respectively. DGFRS-2 separates particles on the basis of their magnetic rigidity: the quantity $B\rho$ determines reaction products, which are guided through the separator to the focal-plane detection system; ρ is determined by the DGFRS-2 design. So for collecting ERs efficiently, one should set the magnetic field in the dipole as follows:

$$B = \frac{m\upsilon}{\rho q}.\tag{2.2}$$

The masses of ERs are known from their decay properties; velocity is determined by the kinematics of the complete fusion reaction, viz, by the momentum conservation law. ERs recoiling from the target are highly ionized (q ≈ 19+ for ^{48}Ca-induced reactions with actinides) and have a

broad charge distribution [7, 8]. In the gas-filled separator, ERs undergo many charge-exchange collisions with dilute gas, which results in a more narrow charge distribution and a decrease in the mean charge to a well-defined equilibrium value ($\approx 6^+$). Due to the high velocity of ^{48}Ca, the charge-exchange cross section in gas is much lower (by about 3–4 orders of magnitude [8]) in comparison to ERs, thereby its mean charge remains close to solid-state value ($\approx 17^+$). At similar momenta, the trajectories of the beam and ERs in the magnetic field differ widely due to a threefold difference in the charges between the beam and ERs.

A fit of the experimentally measured [9] charges in H_2 show a linear dependence of the ER's mean charge on the velocity v (figure 2a):

$$q = 3.26 \cdot \frac{v}{v_0} - 1.39, \tag{2.3}$$

where $v_0 = 2.19 \cdot 10^6$ m/s is the velocity of an electron in the first orbit within the Bohr's model of the hydrogen atom.
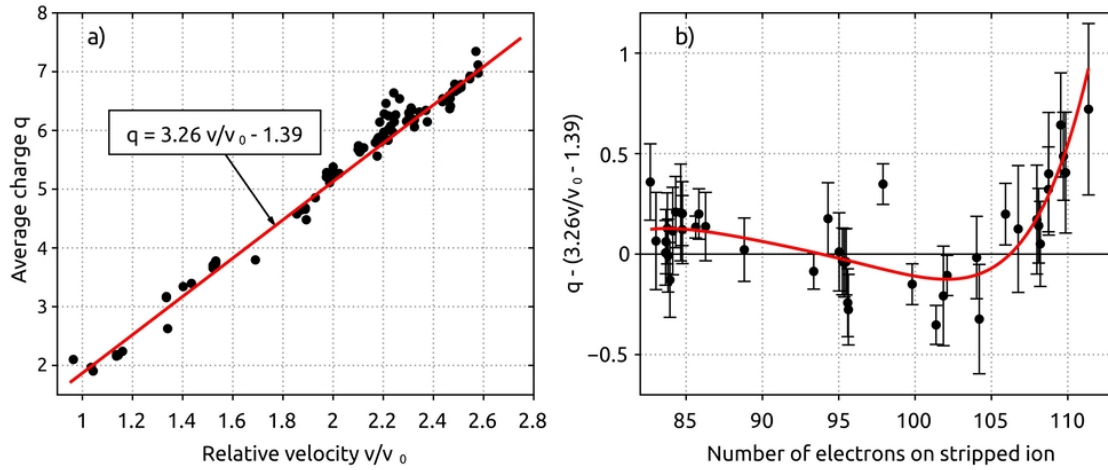

Figure 2. a) Systematics of the measured equilibrium charge states of heavy atoms in dilute hydrogen and their dependence on v/v_0. b) Dependence of shell corrections for elements with $Z = 89$–118 in hydrogen on the number of electrons on a stripped ion.

To achieve high DGFRS-2 collection efficiency, high-precision measurements of a mean equilibrium charge of ERs are of great importance. To calculate the ion charge more accurately, we took into account the deviations of the linear dependence occurring due to shell effects. The polynomial was fitted to the deviations given in figure 2b, and these charge values were used in calculations. The experimental data showed that the dispersion of DGFRS-2 was 32.8 mm/($\%B\rho$) [10]. Thus, a 1% error in the charge of ERs leads to a shift in the distribution of synthesized nuclei in the focal plane by 32.8 mm, thereby resulting in a potential decrease in their collection efficiency.

With due regard for these considerations, a simulation model of DGFRS-2 should include the following processes in order to provide good calculation accuracy:

1. Forming of a compound nucleus in the target layer.

2. Evaporation of several neutrons from a compound nucleus.

3. Modeling of multiple scattering of ERs in the target and other separator's media (filling gas, a Mylar window between the separator and detector volumes, pentane in the detector chamber).

4. Calculation of energy losses in the target and media.

5. Modeling of an ERs recharge process in gas.

6. Calculation of recoil trajectory in the magnetic fields of the separator.

3 Fusion-evaporation process

As was noted in introduction, the heaviest SHEs were produced in hot fusion reactions. The fusion-evaporation process implemented in the model describes the fusion of the beam and target nuclei, leading to the formation of a compound nucleus that subsequently losses the excitation energy and cools down by evaporating several neutrons. The final nucleus continues moving in the target.

The calculations of the trajectories of complete fusion reaction products in DGFRS-2 were performed by GEANT4 using the Monte-Carlo simulation methods. In the first step, the energy of the projectile was randomly generated in accordance with the energy resolution of the ion beam and its spatial distribution on the target surface. When a particle passed through the target backing and target layer, the multiple scattering, energy loss, and energy straggling were taken into account.

In the next stage, the excitation energy of a compound nucleus was randomly generated in accordance with the excitation function of the reaction. The form of the excitation function was gaussian with a full width at half maximum of 10 MeV. Afterwards, based on the range tables [11] and the energy of the projectile after target backing, the coordinate in the target layer was calculated, in which the compound nucleus would have the generated excitation energy. If such a point in the target layer did not exist (generated excitation energy was too high or too low), the excitation energy was generated again. At this point of the target, a compound nucleus was formed with the corresponding excitation energy, which was recalculated from the mass tables [12, 13] and the kinetic energy of the projectile at that point. The initial momentum of the compound nucleus was equal to the momentum of the projectile at the point of generation.

Then we simulated the evaporation of neutrons from the compound nuclei. The kinetic energy of a neutron was generated randomly according to the Maxwell distribution:

$$p(E_n) = E_n e^{\frac{-E_n}{T}}; \quad T = \sqrt{\frac{E^*}{a}}; \quad a = \frac{A}{10}, \tag{3.1}$$

where E_n is the neutron kinetic energy, T is temperature within the Fermi-gas model, a is a level density parameter of the nucleus, A is a mass number of the nucleus, and E^* is the excitation energy.

The neutron momentum distribution was isotropic. The excitation energy of nucleus carried out by neutron was calculated by the formula: $\Delta E_{CN}^* = E_n + E_n^{bind}$, where E_n^{bind} is the binding energy of a neutron in the compound nucleus from the tables in [12, 13]. The momentum of a neutron was added to the initial momentum of the nucleus.

To perform these calculations, a C++ class was written and implemented in GEANT4.

4 Multiple scattering simulation

After analyzing several models proposed by GEANT4, a model described by the class G4ScreenedNuclearRecoil was chosen to estimate multiple scattering [14]. This model reproduces the results of the TRIM calculation [11], a widely used code for modeling the passage of ions through matter. TRIM algorithms for simulating the passage of SHEs through matter are discussed in [15]. TRIM is also used in code [16] for simulating the passage of recoils through the target.

Scattering of two atoms is treated as a completely classical process and is described by the interaction potential:

$$V(r) = \frac{Z_1 Z_2 e^2}{r} \varphi\left(\frac{r}{a}\right), \tag{4.1}$$

where Z_1 and Z_2 are the charge numbers of interacting nuclei, e is an elementary electrical charge, r is a distance between nuclei, φ is a function describing the effect of the electron screening of the nuclear charge, and a is a characteristic screening scale. G4ScreenedNuclearRecoil allows choosing one of several screening functions. The Ziegler-Biersack-Littmark function employed in TRIM was used for simulations.

5 Estimation of energy loss

In passing through the separator, projectiles and superheavy elements synthesized in a complete fusion reaction lose energy due to ionization and excitation of atoms and molecules of media. Energy losses need to be precisely calculated in order to select the optimal values of currents in the separator magnets, which will provide maximum transmission of recoils from the target to the focal plane.

In our work, we used a range tables of heavy ions in matter for calculating ionization losses. The range dependence of SRIM [11] and the Northcliffe-Schilling tables [17] on an ion's proton number was isolated. Linear extrapolation in the SHE region was performed. The fluctuations of energy losses were estimated with a model described by the class G4IonFluctuations.

The calculations on the basis of the SRIM tables agreed well with those performed on the basis of the Northcliffe-Schilling tables used in experiments at DGFRS-1. This allowed us to use the experimental systematics (figure 2) for estimating an average charge value at different energies (velocities) without any modifications.

6 Recharge process

As mentioned in section 2, ERs recoiling from the target are highly ionized with a large average charge and a broad distribution of potential charges. The charge states of ERs have two components: an equilibrated "solid" component [7, 8] and a much higher non-equilibrated component arising from the emission of the Auger-electrons at final stages of de-excitation ([18] and references therein). In order to reduce the average charge, and to narrow the charge distribution, which is important for better focusing of ions by the magnetic elements, the DGFRS-2 chamber is filled with hydrogen. In collisions with hydrogen molecules, ERs lose and capture electrons. The charge distribution of ERs narrows quite rapidly — in rarefied H_2 with a pressure of 1 Torr both components become equilibrated at a distance of 0–12 cm from the target [18]. In the equilibrium state, the charge of

recoils fluctuates among the charge states, affecting the trajectory of motion in magnetic elements and the final distribution of recoils in the focal plane.

Electron-loss and capture cross sections are used to describe the recharge process. The calculation of the cross sections is complicated ab initio. The calculations showed a discrepancy up to 20% between the average values of charge and the experimental results [19] even when using the most advanced theoretical methods. With such an error and a $\approx 30\,\text{mm}/\%B\rho$ dispersion of the separator, the image in the focal plane can be shifted by $\approx 600\,\text{mm}$ relative to the center, which does not allow using the algorithms for determining the optimal parameters of the magnetic elements.

For simulating the recharge process, we thus wrote an algorithm for GEANT4 mostly based on the description of the recharge process given in [8, 16], which uses an experimentally measured average charge value.

This algorithm is based on two principles:

1. The distribution of charges in the equilibrium state is Gaussian.

2. Electron-capture and electron-loss cross sections decrease or increase exponentially with the current recoil charge deviating from equilibrium. Multi-electronic recharge is neglected.

An equilibrium value of the charge was calculated from linear systematics (3) with due regard for shell corrections [9] (figure 2b). The capture cross section for this charge was calculated using an exponential dependence proposed in [20]. The results agreed well with the experimental data for the energy range of ions under investigation [18]:

$$\sigma_{\text{fit}} = a_c \overline{q} \exp(b_c E_r), \tag{6.1}$$

where $\overline{q}$ is a charge equilibrium, $E_r = E/\overline{q}^{\frac{4}{7}}$, E is the ER kinetic energy in keV per nucleon, a_c and b_c are constants obtained from the fit [18], $a_c = 8.77$, $b_c = -0.0614$.

From the two principles we outlined above, it follows that for the equilibrium charge the electron-capture cross section is equal to the electron-loss cross section. Therefore, the capture and loss cross sections for different charge states can be calculated from the capture cross section for the average charge:

$$\sigma_{q,q-1} = \sigma_{\text{fit}} \exp(c_c(q - \overline{q})), \tag{6.2}$$

$$\sigma_{q,q+1} = \sigma_{\text{fit}} \exp(c_c(\overline{q} - q)), \tag{6.3}$$

where q is an ER charge, $c_c = 0.12$ — was found empirically on the basis of the measured dependence of the width of the ER distribution in the focal plane on hydrogen pressure.

Finally, the capture probability is calculated with the formula as $p_{\text{capture}} = \frac{\sigma_{q,q-1}}{\sigma_{q,q-1}+\sigma_{q,q+1}}$, and capture or loss of an electron are generated.

To perform calculations, a class was written for GEANT4 on the basis of the G4DiscreteModel class.

7 Movement in magnetic fields

In order to propagate an ion inside a field, an equation of motion for the particle in the field was integrated. This is routinely done using the Runge-Kutta method for the integration of ordinary

differential equations. In our calculations, we used the Dormand-Prince scheme of the Runge-Kutta method implemented in the G4DormandPrince745 class.

Once a method for the calculation of an ion trajectory in a specific field was chosen, the curved path was broken up into linear chord segments, which were determined so that they closely approximated the curved path. Several parameters were available to adjust the accuracy of integration and subsequent interrogation of the model geometry. Three of them were relevant to integration accuracy. The parameter DeltaOneStep was roughly a position error acceptable in an integration step. The next two parameters imposed a further limit on the relative error of the position/momentum inaccuracy. DeltaOneStep was dominated by EpsilonMin and EpsilonMax that imposed a minimum and maximum on the relative error [21].

We used magnetic field maps calculated in the OPERA-3D program. In our calculations, we employed three-dimensional models of magnets created by SIGMAPHI during the design phase of the DGFRS-2 magnetic components. The magnetic field maps were calculated with a 5-mm step and trilinearly interpolated for obtaining values between the grid nodes.

In order to perform calculations, a class was written for GEANT4, which reads the field map for the required electrical current of the DGFRS-2 magnets and creates necessary subclasses.

8   Results of calculation

In studying of characteristics of the DGFRS-2 separator, a number of test experiments [10] with the ^{174}Yb(^{48}Ca,5n)^{217}Th and ^{206}Pb(^{48}Ca,2n)^{252}No reactions were performed. Widths of the targets were 0.35 mg/cm^2 for Yb$_2$O$_3$ and 0.43 mg/cm^2 for PbS. In figure 3 are presented the horizontal and vertical trajectory profiles for ^{252}No recoils. In addition, we measured the effect of currents in quadrupole lenses on the image size in the focal plane. In order to achieve the maximum probability for nuclei to reach the surface of the existing detector, it is necessary that the standard deviations of their vertical and horizontal distributions should be minimal and would not exceed a fourth of the corresponding detector size. This allows a collection of 95% of nuclei in each direction. However, due to a relatively large dispersion of the separator, we needed to search for an optimal ratio of the distribution widths and currents in Q2 and Q3 for attaining the maximum probability of collecting nuclei in detectors. The widths of the horizontal and vertical distributions of ^{217}Th and ^{252}No were measured at different field gradients in the lenses Q2 and Q3. For ^{217}Th and ^{252}No, five and three different field values, respectively, were selected for Q2. Three Q3 values were used for each of the Q2 values. The distributions of nuclei in the detectors were fitted by the Gaussian function; their standard deviations are shown in figure 4. The Q2 values are depicted in the figures, the data are given in correlation to the corresponding values of Q3. The same figure shows the results of simulations. The results of calculations agreed well with the experimental data. As can be seen from figure 4, the minimum vertical distribution widths do not always coincide with the minimum horizontal widths.

To achieve the optimal tuning, the program searches for the values of currents in Q2 and Q3 at which the maximum number of produced nuclei hits the detector surface. In the experiment, the optimal Q2-Q3 ratios were determined by searching for a maximum yield of nuclei for which the number of nuclei per beam dose was taken for all Q2-Q3 combinations. Figure 5 shows the yields of nuclei at different Q2-Q3, each of the Q2-Q3 ratios corresponding to its local maximum yield. As a result, the maximum yield was found. In figure 5, we see that the measured yields are in good
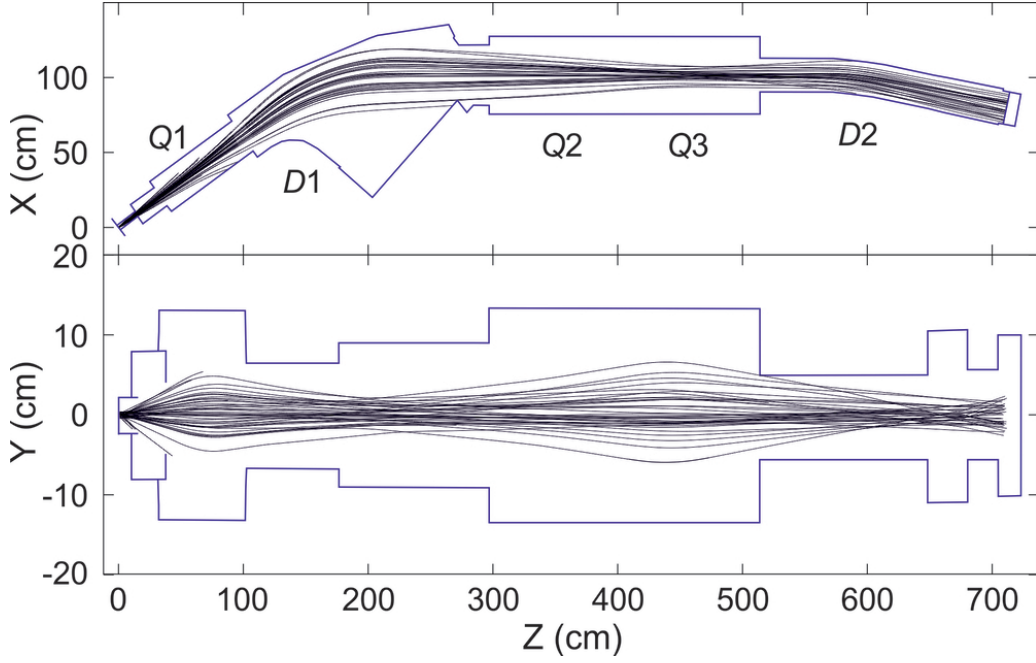
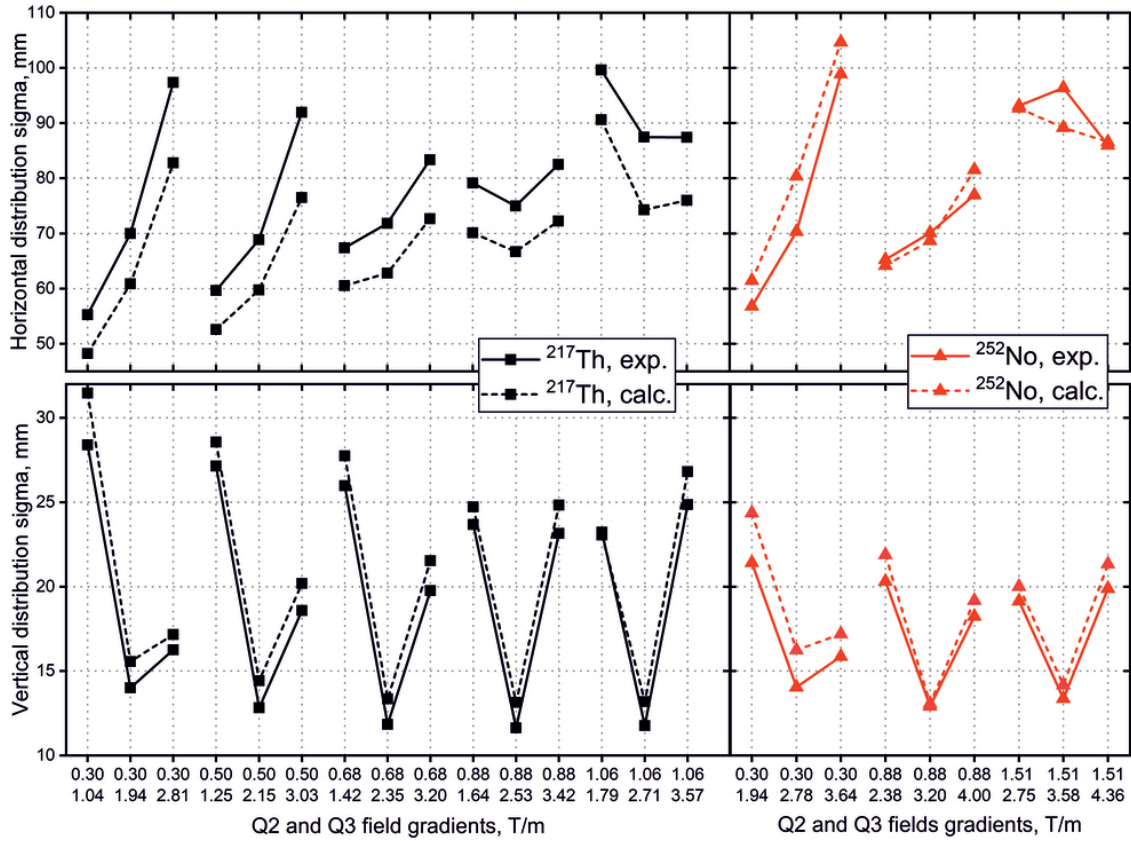**Figure 3**. Simulated trajectories of ^{252}No produced in the ^{206}Pb(^{48}Ca,2n)^{252}No reaction.

Figure 4. Comparison of the experimental and calculated image widths for the ^{174}Yb(^{48}Ca, 5n)^{217}Th and ^{206}Pb(^{48}Ca,2n)^{252}No reactions at different field gradients in Q2 and Q3.
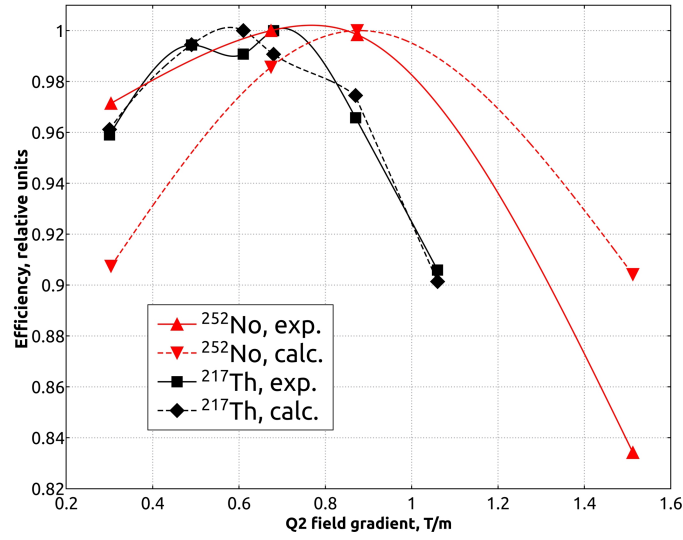
Figure 5. Comparison of relative efficiencies of the ^{174}Yb(^{48}Ca, 5n)^{217}Th and ^{206}Pb(^{48}Ca,2n)^{252}No reactions. An experimentally found optimal Q3 field gradient was used for each of the Q2 field gradients.
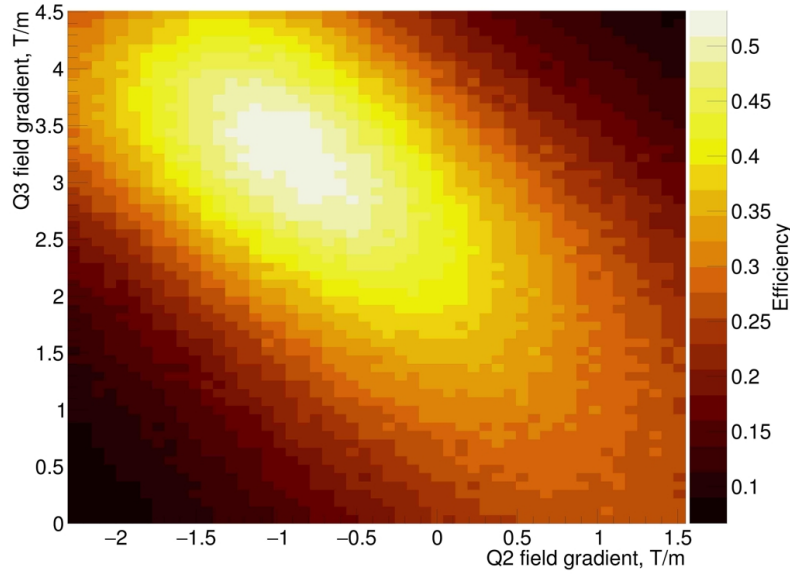

Figure 6. A search for an optimal Q2-Q3 combination for the ^{206}Pb(^{48}Ca,2n)^{252}No reaction with target width of 0.43 mg/cm^2. The negative field gradient corresponds to a horizontally focusing quadrupole, whilst the positive field gradient corresponds to a vertically focusing quadrupole. Collection efficiency for the focal-plane detector of 220×48 mm^2 is marked in colors.

agreement with the experimental data. Figure 6 shows the calculated dependence of the collection efficiency on the fields in Q2 and Q3 for the ^{206}Pb(^{48}Ca,2n)^{252}No reaction, thereby allowing the use of the developed model for determining the optimal values of currents in quadrupoles for reactions leading to the formation of SHEs.

The calculations of the current in the first quadrupole Q1 cannot be verified in the same way: a change in the current in the first quadrupole does not affect the shape of the image in the focal plane, only the recoil collection efficiency is influenced. In determining an optimal value experimentally, we thus used the number of registered recoils divided by the beam dose and compared it with the calculated efficiency collection in the focal plane. The experimental and calculated yields of ^{217}Th and ^{252}No presented in figure 7 in relative units showed good agreement with the data on the ^{174}Yb(^{48}Ca,5n)^{217}Th reaction. The discrepancy for the ^{206}Pb(^{48}Ca,2n)^{252}No reaction at Q1 = 7 T/m is largely due to inaccuracy in the dose measurement.
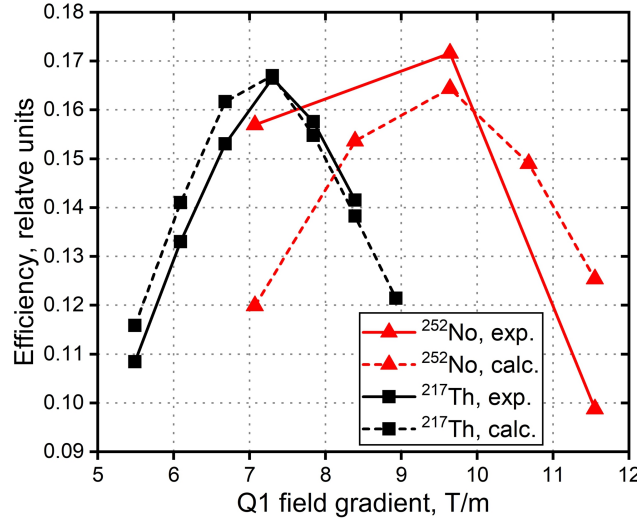

Figure 7. Comparison of the experimental and calculated relative efficiencies for the ^{174}Yb(^{48}Ca, 5n)^{217}Th and ^{206}Pb(^{48}Ca,2n)^{252}No reactions at different field gradients in Q1.

The effect of hydrogen pressure on the size of the image in the focal plane was also experimentally studied [10]. In the model, we did not take into account the density effect that influenced the absolute value of the average charge in a gas [8]. Taking into consideration the recharge process, however, we were able to describe with satisfactory accuracy the changes in the image size at the focal plane, which occurred due to a change in the free path length between charge-changing collisions. At a low pressure due to rarer interactions with gas atoms resulting in transitions between the charge states, the average charge distribution width in the magnetic field increases, which leads to an increase in the image width in the dispersive (horizontal) direction. As pressure increases, the time between collisions decreases, reducing the width of the charge distribution and a corresponding width of image. As pressure further increases, multiple scattering gives contribution, which in turn increases the image size both in dispersive and non-dispersive directions. A comparison of the measured [10] and calculated widths of the distributions for ^{217}Th and ^{252}No at different H_2 pressures in DGFRS-2 is presented in figure 8. We can see that the model reproduces the experimental data fairly well.

An important characteristic of the separator is magnetic dispersion defined as a shift of the center of the horizontal distribution (when the magnetic field changes) and expressed in mm per percent of change in the magnetic rigidity $\Delta X/\Delta B\rho$. A good agreement was observed for the separator dispersion: the calculated value was 33.1 ± 0.4 mm/%$B\rho$, whereas the measured value was 32.8 ± 0.3 mm/%$B\rho$ [10].
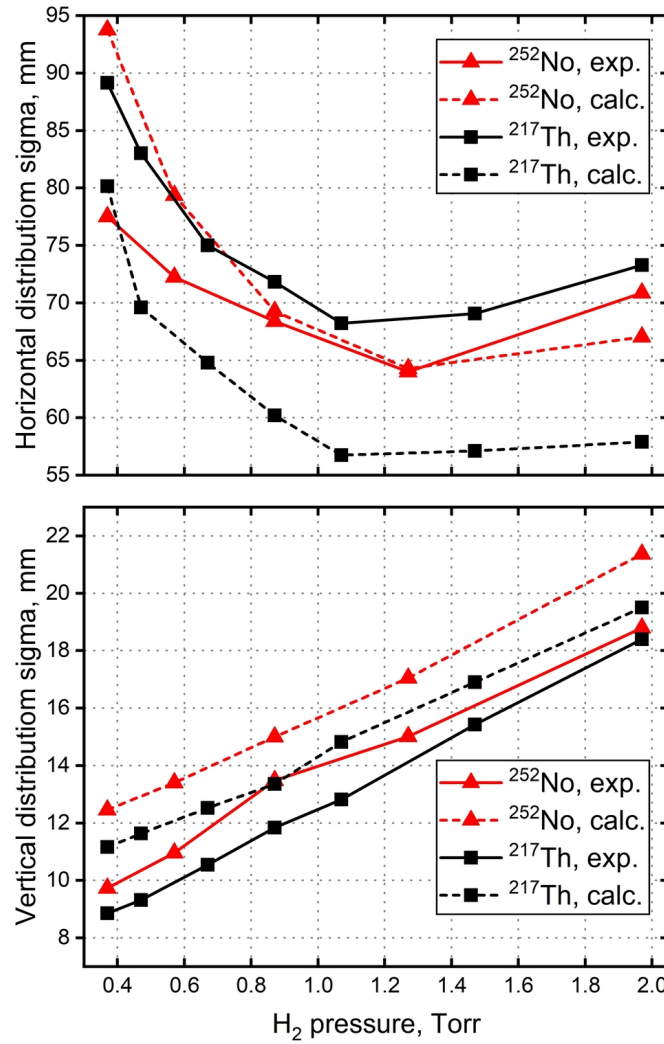
Figure 8. Dependence of image size on H_2 pressure.

With such a dispersion of DGFRS-2, the accuracy of predicting the position of the distribution maximum of ions at the focal plane will depend on the accuracy of the measured value of their average charge. For some ions, the accuracy of the charge may be up to 3% and more, leading to an uncertainty in the position of their maximum in detectors up to 100 mm. Taking this fact into consideration, the horizontal size of the focal detector of DGFRS-2 was increased to 220 mm. The new design of the detector chamber implies an increase in the detector size from 220×48 to 240×60 mm.

The calculated transmission of the separator, defined as a ratio of ^{252}No nuclei that reached the focal plane to the number of nuclei produced in the reaction of 0.43-mg/cm^2 ^{206}Pb with ^{48}Ca, was 61%, which agreed well with an experimentally obtained value of $59 \pm 7\%$ [10]. Good agreement allows us to use the calculated efficiency for determining cross sections for the production of SHEs.

The transmission of the separator and the number of ERs that can reach its focal plane strongly

depend on the thickness of the target layer. As the thickness increases, transmission decreases since most part of the nuclei are lost in the walls of the separator chamber due to multiple scattering in the target. However, the total number of produced nuclei increases almost linearly (taking into account the reaction excitation function) with increasing target thickness. Thus, the total number of nuclei reaching the focal plane increases with increasing target thickness. Figure 9 shows a comparison of calculated data on transmission and the yield of ERs for the ^{244}Pu(^{48}Ca,4n)^{288}Fl reaction during the design development phase [5] and using the GEANT4 model. The yield of nuclei depicted in relative units was calculated as a product of transmission and the target thickness [5]. The calculated data using the GEANT4 model were consistent with the design values [5].
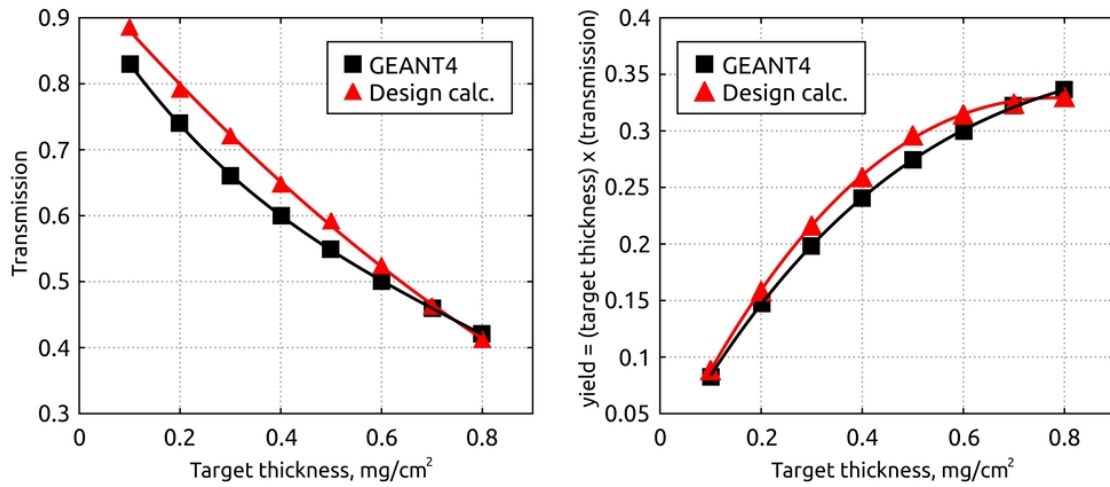

Figure 9. Comparison of design simulations [5] of transmission (left panel) and yield (right panel) with GEANT4 model.

9 Conclusion

Using the GEANT4 toolkit, a model was created for calculating the trajectories of recoils in the DGFRS-2 separator, taking into account the complex geometry of the gas-filled chamber. In order to perform calculations, several C++ classes were written to simulate the following physical processes: a process of complete fusion followed by an evaporation of several neutrons, energy losses of nuclei in DGFRS-2, their multiple scattering, a recharge process of recoils in dilute hydrogen, and motion in magnetic fields. In order to compare with results of test experiments, several combinations of the ^{174}Yb(^{48}Ca,5n)^{217}Th and ^{206}Pb(^{48}Ca,2n)^{252}No reactions with different electrical currents in the DGFRS-2 magnets and hydrogen pressure were simulated. The focal plane distributions of ERs varying with pressure and electrical current in magnets were obtained and analyzed. The calculated and experimentally estimated results were in good agreement, which allowed us to use the developed model for calculating the optimal magnetic fields in experiments on the synthesis of SHEs. In addition, the high flexibility of the created model allowed us to use these algorithms in the development of new gas-filled and vacuum setups for the SHE Factory.

Acknowledgments

References

[1] Y. Oganessian, *Heaviest nuclei from ^{48}Ca induced reactions*, *J. Phys. G* **34** (2007) R165.

[2] Y.T. Oganessian and V.K. Utyonkov, *Superheavy nuclei from ^{48}Ca-induced reactions*, *Nucl. Phys. A* **944** (2015) 62.

[3] Y.T. Oganessian and V.K. Utyonkov, *Super-heavy element research*, *Rep. Prog. Phys.* **78** (2015) 036301.

[4] G.G. Gulbekian et al., *Start-Up of the DC-280 Cyclotron, the Basic Facility of the Factory of Superheavy Elements of the Laboratory of Nuclear Reactions at the Joint Institute for Nuclear Research*, *Phys. Part. Nucl. Lett.* **16** (2019) 866.

[5] A. Popeko, *On-line separators for the Dubna Superheavy Element Factory*, *Nucl. Instrum. Meth. B* **376** (2016) 144.

[6] J. Allison et al., *Recent developments in Geant4*, *Nucl. Instrum. Meth. A* **835** (2016) 186.

[7] G. Schiwietz and P. Grande, *Improved charge-state formulas*, *Nucl. Instrum. Meth. B* **175-177** (2001) 125.

[8] H.-D. Betz, *Charge states and charge-changing cross sections of fast heavy ions penetrating through gaseous and solid media*, *Rev. Mod. Phys.* **44** (1972) 465.

[9] Y.T. Oganessian et al., *Average charge states of heavy atoms in dilute hydrogen*, *Phys. Rev. C* **64** (2001) 064309.

[10] Y. Oganessian, V. Utyonkov, A. Popeko, D. Solovyev, F. Abdullin, S. Dmitriev et al., *DGFRS-2 — a gas-filled recoil separator for the Dubna Super Heavy Element Factory*, *Nucl. Instrum. Meth. A* **1033** (2022) 166640.

[11] J.F. Ziegler, M. Ziegler and J. Biersack, *SRIM – the stopping and range of ions in matter (2010)*, *Nucl. Instrum. Meth. B* **268** (2010) 1818.

[12] M. Wang, G. Audi, F.G. Kondev, W. Huang, S. Naimi and X. Xu, *The AME2016 atomic mass evaluation (II). tables, graphs and references*, *Chin. Phys. C* **41** (2017) 030003.

[13] W.D. Myers and W. Swiatecki, *Average nuclear properties*, *Ann. Phys.* **55** (1969) 395.

[14] M.H. Mendenhall and R.A. Weller, *An algorithm for computing screened coulomb scattering in Geant4*, *Nucl. Instrum. Meth. B* **227** (2005) 420.

[15] R. Sagaidak, V. Utyonkov and F. Scarlassara, *Simulation of angular and energy distributions for heavy evaporation residues using statistical model approximations and TRIM code*, *Nucl. Instrum. Meth. A* **700** (2013) 111.

[16] K. Gregorich, *Simulation of recoil trajectories in gas-filled magnetic separators*, *Nucl. Instrum. Meth. A* **711** (2013) 47.

[17] L.C. Northcliffe and R.F. Schilling, *Range and stopping-power tables for heavy ions*, *Atom. Data Nucl. Data Tabl.* **7** (1970) 233.

[18] R.N. Sagaidak, *Empirical relations for heavy-ion equilibrated charges and charge-changing cross sections in diluted H_2 with application*, *Eur. Phys. J. D* **75** (2021) 220.

[19] J. Khuyagbaatar, V.P. Shevelko, A. Borschevsky, C.E. Düllmann, I.Y. Tolstikhina and A. Yakushev, *Average charge states of heavy and superheavy ions passing through a rarified gas: Theory and experiment*, *Phys. Rev. A* **88** (2013) 042703.

[20] H. Knudsen, H.K. Haugen and P. Hvelplund, *Single-electron-capture cross section for medium- and high-velocity, highly charged ions colliding with atoms*, *Phys. Rev. A* **23** (1981) 597.

[21] *Geant4 book for application developers, Detector definition and response, Electromagnetic field*, https://geant4-userdoc.web.cern.ch/UsersGuides/ForApplicationDeveloper/html/Detector/electroMagneticField.html (2022).